Heterostructured CdS Buffer Layer for Sb_2Se_3 Thin Film Solar Cell

Al Amin, Xiaomeng Duan, Jacob Wall, Kausar Ali Khawaja Wenjun Xiang, Lin Li, Feng Yan*[1]

Materials Science Program, School for Engineering of Matter, Transport and Energy, Arizona State University, Tempe, AZ, 85287, USA

Abstract:

The antimony selenide (Sb_2Se_3) thin film solar cells technology become promising due to its excellent anisotropic charge transport and brilliant light absorption capability. Especially, the device performance heavily relies on the vertically oriented Sb_2Se_3 grain to promote photoexcited carrier transport. However, crystalline orientation control has been a major issue in Sb_2Se_3 thin film solar cells. In this work, a new strategy has been developed to tailor the crystal growth of Sb_2Se_3 ribbons perpendicular to the substrate by using the structural heterostructured CdS buffer layer. The heterostructured CdS buffer layer was formed by a dual layer of CdS nanorods and nanoparticles. The hexagonal CdS nanorods passivated by a thin cubic CdS nanoparticle layer can promote [211] and [221] directional growth of Sb_2Se_3 ribbons using a close space sublimation approach. The improved buffer/absorber interface, reduced interface defects, and recombination loss contribute to the improved device efficiency of 7.16%. This new structural heterostructured CdS buffer layer can regulate Sb_2Se_3 nanoribbons crystal growth and pave the way to further improve the low-dimensional chalcogenide thin film solar cell efficiency.

Keywords: Thin film solar cell, Sb_2Se_3, Heterostructured CdS buffer layer, Power conversion efficiency

---

[1] fengyan@asu.edu

1. Introduction

Solar cell technology provides renewable energy to address the fossil fuel-related energy crisis and climate change.[1] Especially, exploring eco-friendly, low-cost, abundant materials has been crucial for the next generation of thin film solar cells. To date, the low toxic and earth-abundant antimony selenide (Sb_2Se_3) has been considered a very promising light absorber material with theoretical high-efficiency solar cell due to its excellent optoelectronic property with an appropriate bandgap of 1.10-1.30 eV, anisotropic charge transport, high light absorption coefficient ($>10^5$ cm^{-1}), and stable orthorhombic phase.[2, 3, 4, 5]

Sb_2Se_3 has a quasi-1D orthorhombic crystalline structure made of ribbon-like $(Sb_4Se_6)_n$ units bonded by van der Waals (vdW) attraction.[3, 6] The photovoltaic (PV) performance of the Sb_2Se_3 solar cell largely depends on the crystal orientation of $(Sb_4Se_6)_n$ ribbons and film morphology. For higher carrier mobility and effective charge collection, the ribbons grown along [211] and [221] direction is imperative rather than [120] because the charge carrier needs to hop between $(Sb_4Se_6)_n$ ribbons held by vdW forces in case of [120] i.e., horizontal grain growth which reduces the electron diffusion length resulting higher recombination.[7, 8] Over the last decade, the Sb_2Se_3 solar cell has significantly improved its power conversion efficiency from 2.6% to 10.12%.[9, 10] However, it still lags behind the theoretical efficiency of > 30% due to high recombination sites at the buffer/absorber interface and space charge region (SCR), and undesired crystal orientation.[6, 11] To fill the gap in its theoretical efficiency limit, several attempts have been done to optimize the buffer/absorber interface and update the buffer layer types to obtain desired materials and electronic properties. For example, $SbCl_3$ treated CdS [12], and Se, Sb_2Se_3, and Sb_2S_3 seeds layer grown on the CdS buffer have been used to tailor the Sb_2Se_3 grain orientation.[4, 13, 14, 15] In addition, various buffer layers have been evaluated for Sb_2Se_3 solar cells. For instance, the $Cd_xZn_{1-x}S$ buffer was used for Sb_2Se_3 solar cell to modify the buffer/absorber band alignment by changing the Cd/Zn ratio in $Cd_xZn_{1-x}S$ synthesis.[16] Besides, TiO_2, SnO_2, ZnO, or dual buffers achieved efficiency of 3.8%, 3.05%, and 6% respectively.[5, 12, 17, 18, 19] Among all these buffers, CdS is still the most efficient buffer layer for the Sb_2Se_3 solar cell, and it has been able to achieve the highest efficiency of 10.12% in substrate device structure so far.[10] However, the cubic zinc-blend structure of the CdS nanoparticles buffer layer has a large lattice mismatch and distortion with orthorhombic Sb_2Se_3.[12]

So far, the hexagonal CdS nanorods have not been used to explore the Sb_2Se_3 solar cell yet. Hexagonal CdS nanorods preferentially grow along [001] direction which can assist the vertical growth of Sb_2Se_3 ribbons.[20] In this work, we have successfully deposited nanorods CdS layer to guide Sb_2Se_3 film growth by close space sublimation (CSS) deposition process. The nanorods CdS combined with nanoparticles CdS passivation layer form a heterostructured CdS buffer layer that can assist Sb_2Se_3 grain growth along [211] and [221] directions. Particularly, the newly formed heterostructured CdS buffer layer can also improve charge transport along CdS nanorods and Sb_2Se_3 ribbons, leading to higher charge recombination resistance and enhancing device performance with a champion efficiency of 7.16%. This structural heterostructured CdS buffer layer can efficiently guide the crystalline growth and promote the device performance in low dimensional chalcogenides thin film solar cells.

2. Results and Discussion

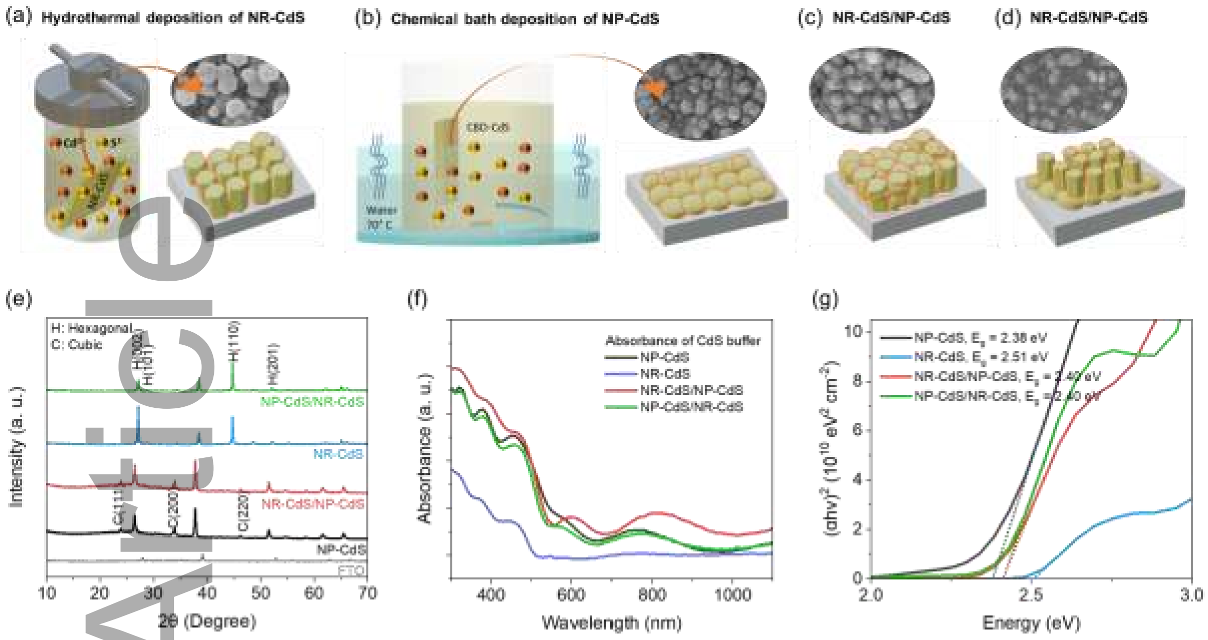

Figure 1. (a-d) Schematic of the synthesis process of structural heterostructured CdS buffers: (a) hydrothermal deposition of CdS nanorods (NR-CdS), (b) conventional chemical bath deposition of CdS nanoparticles (NP-CdS), (c) heterostructured NR-CdS/NP-CdS, (d) heterostructured NP-CdS/NR-CdS (e) XRD patterns, (f) optical absorbance, and corresponding (g) bandgap calculated from Tauc plot of these CdS buffer layers.

Figure 1a and b show the schematic of the deposition process and crystal structure of CdS nanorod and nanoparticles prepared by hydrothermal and CBD method, respectively. Figure 1c shows the heterostructured NR-CdS/NP-CdS buffer layer, where the NP-CdS was deposited on the NR-CdS nanorods. Reversely, the heterostructured NP-CdS/NR-CdS buffer layer as shown in Figure 1d was fabricated by depositing NR-CdS on the CBD deposited NP-CdS buffer. The thickness of these nanorods and nanoparticles CdS was controlled by the deposition time. The crystal structure of these CdS buffer layers was determined using X-ray diffraction (XRD) as shown in Figure 1e. It is shown that the traditional chemical bath deposited nanoparticles CdS buffer layer possesses a cubic structure, while the nanorod CdS layer has a hexagonal structure. The crystalline of the heterostructured CdS buffer layer follows the top layer structure. For example, the NR-CdS/NP-CdS buffer layer shows the cubic structure of the NP-CdS, while the NP-CdS/NR-CdS buffer layer presents the hexagonal structure. Figure 1f and g display the light absorbance spectra and corresponding calculated optical bandgap. The CBD-deposited NP-CdS shows a bandgap of 2.38 eV which is in agreement with the reported bandgap.[21] The NR-CdS shows a comparatively higher bandgap of 2.51 eV. However, the bandgap of heterostructured NR-CdS/NP-CdS and NP-CdS/NR-CdS reduces to 2.40 eV, suggesting that the heterostructured CdS buffer layer still shows great light transmittance as a window layer.

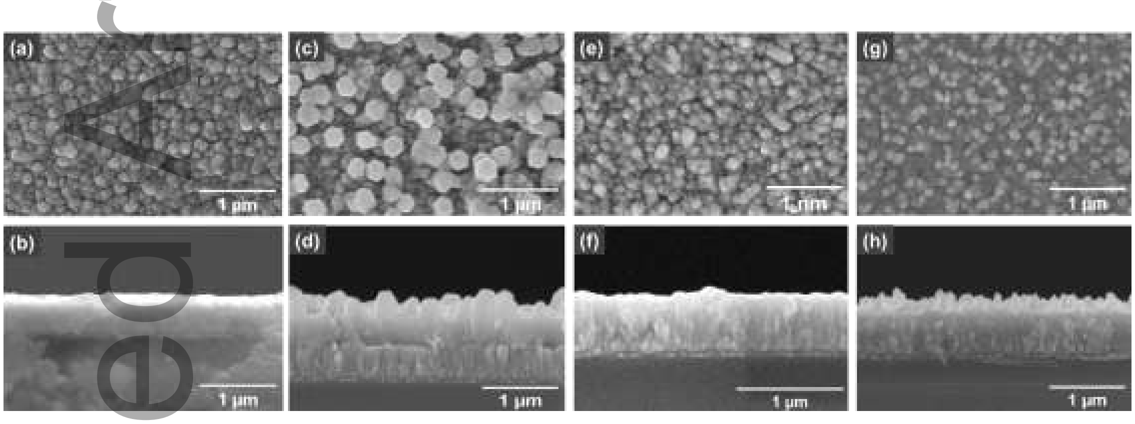

Figure 2. SEM surface morphology and cross-sectional images of different CdS buffers grown on FTO substrate: (a-b) NP-CdS, (c-d) NR-CdS, (e-f) NR-CdS/NP-CdS, and (g-h) NP-CdS/NR-CdS, respectively.

Figure 2a-h displays the surface morphology and cros-section of the NP-CdS, NR-CdS, NR-CdS/NP-CdS, and NP-CdS/NR-CdS respectively. The CBD-deposited CdS shows densely packed nanoparticles with grain size ~100 nm (Figure 2a), while the hydrothermal deposited CdS nanorod shows hexangular nanorods like crystal shape (with a diameter of~ 200 nm) grown vertically on the FTO substrate. The CBD of CdS is done at atmospheric pressure and comparatively lower temperature. During CBD process, the $CdSO_4$ and thiourea releases Cd^{2+} cations and S^{2-} anions respectively, which attracts eatch other and form CdS molecules. These

CdS molecules then deposit on the substrate and create CdS nanoparticles layer.[22] Conversely, the hydrothermal deposition of CdS is done at higher pressure and temperature. Glutathione is added with Cd and S source materials in hydrothermal reaction where the thiol and dicarboxyl groups in glutathione works as capping agent to grow the hexagonal CdS nanorods.[23] However, the top surface of these CdS nanorods for both the pure CdS nanorod and the heterostructured NP-CdS/NR-CdS are packed loose on the FTO substrate, which leads to a rough surface for the following Sb_2Se_3 layer deposition. To avoid this problem, CdS nanoparticles were deposited on the NR-CdS film to fill the gaps of the CdS nanorod to form a dense heterostructured NR-CdS/NP-CdS buffer for the Sb_2Se_3 deposition, as shown in Figure 2e-f.

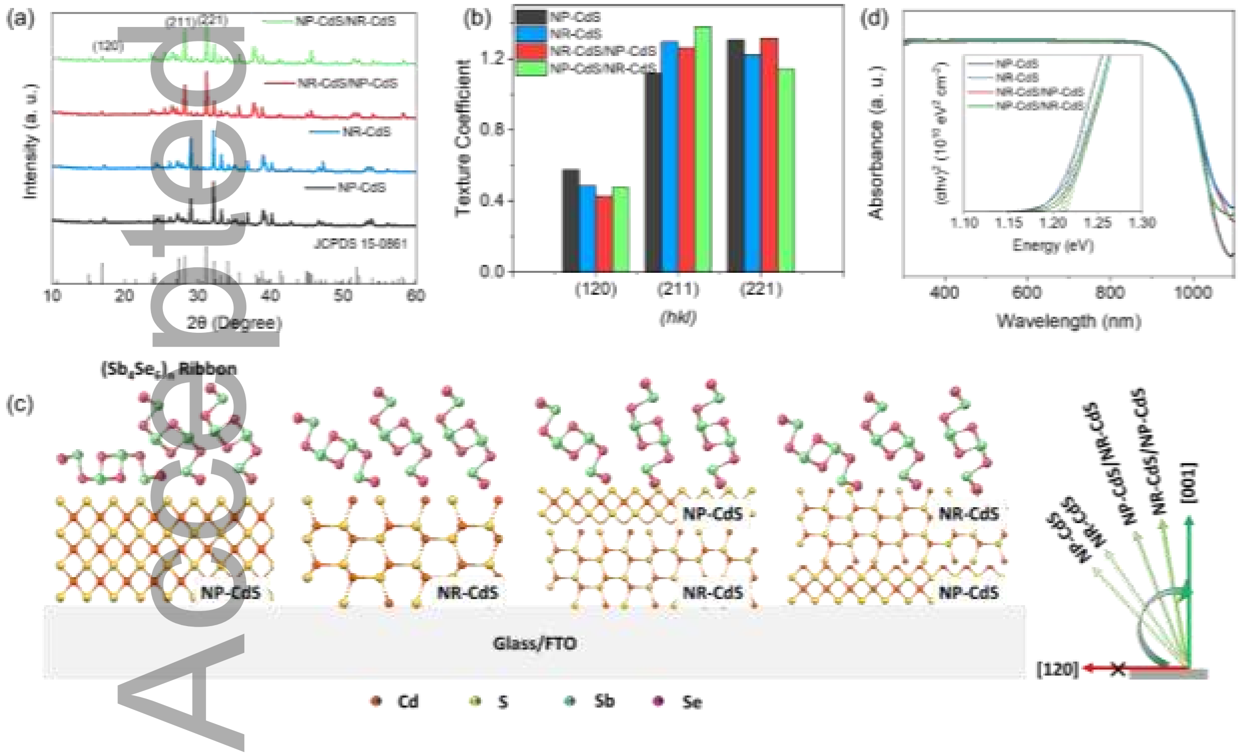

Figure 3. Crystalline and optical properties of the Sb_2Se_3 thin film deposited on different CdS buffers. (a) XRD patterns, corresponding calculated (b) texture coefficient and (c) schematic of the Sb_2Se_3

nanoribbons preferred growth orientation on various CdS buffers, and (d) optical absorbance and calculated bandgap from Tauc plot (inset).

We employ the CSS approach to deposit the Sb_2Se_3 absorber layer on the various CdS buffer layers.[24] Figure 3a shows the XRD patterns of the as-deposited Sb_2Se_3 films on the various CdS buffers, and standard XRD patterns of Sb_2Se_3 (JCPDS 15–0861). All the as-prepared Sb_2Se_3 films exhibit the orthorhombic crystal structure of the Pbnm space group with no other noticeable impurities.[24] As shown in Figure 3b, the calculated textured coefficient (TC) of these Sb_2Se_3 films [2] suggests that NR-CdS and NR-CdS/NP-CdS buffer layer promote the vertical growth of Sb_2Se_3, where the TC of (120)-orientation reduced and TC of (211)-orientation increased. The hexagonal nanorods CdS promote the vertical growth of Sb_2Se_3 ribbons that matches the previously found results published in [12]. Particularly, The NR-CdS/NP-CdS has a larger TC of (211) than that of the pure NP-CdS, implying that Sb_2Se_3 nanoribbons grown on NR-CdS/NP-CdS are more vertical than grown on only NP-CdS buffer layer. For a better understanding of preferred crystal orientation based on TC, a schematic of Sb_2Se_3 ribbons growth and their relative average growing direction has been presented in Figure 3c. The absorbance spectra of the Sb_2Se_3 films have been delineated in Figure 3d, which shows similar light absorbance characteristic from wavelength of 300 nm to 1000 nm except slight changes over 1000 nm. The optical bandgap calculated by Tauc plot has been presented in Figure 3d (inset), all Sb_2Se_3 films show almost same bandgap of 1.21 eV.

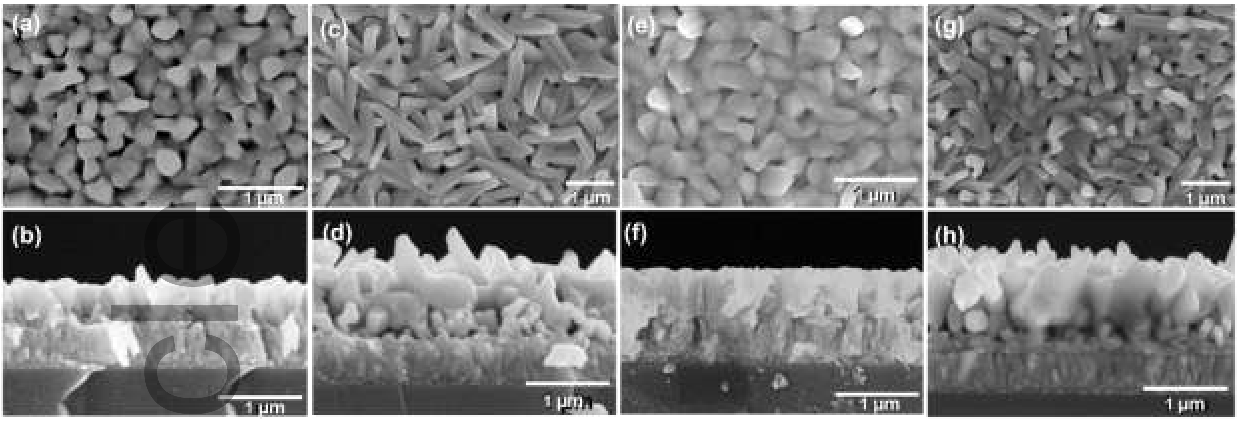

Figure 4. SEM surface and corresponding cross-section morphologies of the Sb_2Se_3 thin film deposited on various CdS buffer layers. (a, b) NP-CdS, (c, d) NR-CdS, (e, f) NR-CdS/NP-CdS, (g, h) NP-CdS/NR-CdS.

The top surface view and corresponding cross-section SEM images of as-deposited Sb_2Se_3 films grown on the various CdS buffer layers are shown in Figure 4. The surface of Sb_2Se_3 film deposited on the NP-CdS buffer shows the granular grain (Figure 4a-b), while the surface of Sb_2Se_3 film deposited on the NR-CdS buffer shows Sb_2Se_3 nanorods (Figure 4c-d), suggesting that the buffer layer significantly influences the growth behavior of the Sb_2Se_3 film. Particularly, the Sb_2Se_3 nanorod surface is pretty rough compared to the Sb_2Se_3 grown on the CdS nanoparticles (Fig. 4b, 4d). As expected, the Sb_2Se_3 films grown on the heterostructured CdS buffer layer show a similar growth behavior as those of the pure NP-CdS. The surface morphology and cross-section of the Sb_2Se_3 grown on NR-CdS/NP-CdS (Figure 4e-f), shows a smooth surface, and compact vertical crystal growth of Sb_2Se_3, while the Sb_2Se_3 film grown on NP-CdS/NR-CdS buffer layer still present considerable nanorods on the surface resulting in rough Sb_2Se_3 surface. This suggests that heterostructured NR-CdS/NP-CdS buffer can succeed in both the high-quality buffer/absorber interface and desired crystallinity for the Sb_2Se_3 layer.

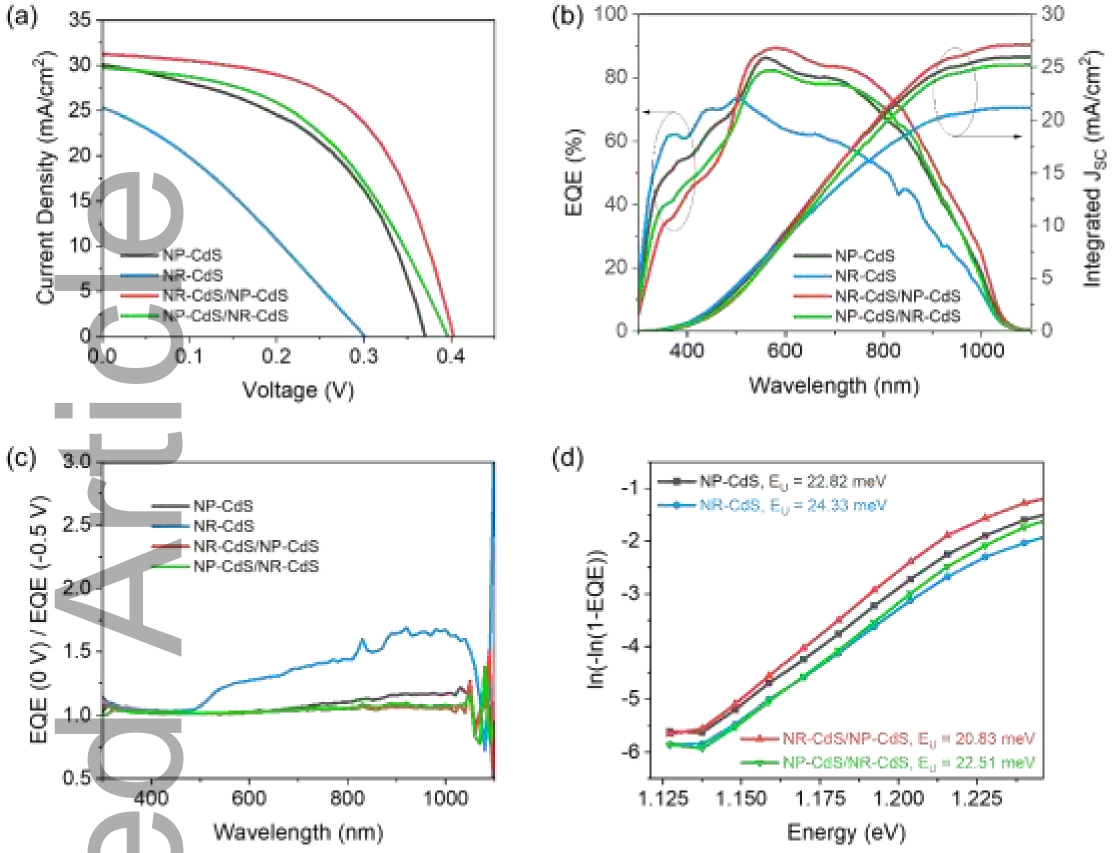

Figure 5. The device performance of Sb_2Se_3 solar cells based on different CdS buffers: (a) *JV* curve under AM 1.5 G illumination (b) EQE spectra and (c) ratio of EQE(−0.5 V)/EQE(0 V) curves of the solar cells, (d) Urbach energy derived from the EQE data of devices.

Figure 5a shows the current density versus voltage curve of Sb_2Se_3 solar cells based on NP-CdS, NR-CdS, NR-CdS/NP-CdS, and NP-CdS/NR-CdS buffers. The champion device for each CdS buffer layer is listed in Table 1. The heterostructured NR-CdS/NP-CdS buffer layer-based device demonstrates the best power conversion efficiency (PCE) of 7.16%, with an open-circuit voltage (V_{OC}) of 0.403V, short-circuit current density (J_{SC}) of 31.16 mA/cm^2, and fill factor (FF) of 57%. After coating the nanoparticles CdS on the nanorods CdS, it fills up the interstitial gap among the

CdS nanorods, which protects the current leakage and recombination that reflects into higher shunt resistance of 185.13 Ω cm^2 and V_{OC} of 0.403V. Furthermore, the CdS nanorods in NR-CdS/NP-CdS structure help easy carrier transportation, which reflects in lower series resistance of 2.59 Ω cm^2 and higher J_{SC} of 31.16 mA/cm^2. This significant performance improvement in NR-CdS/NP-CdS device can be attributed to the high-quality Sb_2Se_3 film with fewer pinholes, compact structure with smother surface, and preferred (211) and (221) crystal orientation confirmed by XRD data analysis (Figure 3a-c).[25] The NR-CdS solar cell shows an overall poor PCE of 2.35% with an V_{OC} of 0.30 V, J_{SC} of 25.21 mA/cm^2, and FF of 31.07% due to the poor interface quality between NR-CdS and Sb_2Se_3. The NR-CdS/NP-CdS devices perform better than the control NP-CdS device.

Table 1. Sb_2Se_3 solar cell photovoltaic performance parameters based on different CdS buffers.

Devices	**V_{OC} (V)**	**J_{SC} (mA/cm^2)**	***FF* (%)**	***PCE* (%)**	**R_S (Ω cm^2)**	**R_{SH} (Ω cm^2)**	**E_U (meV)**
NP-CdS	0.37	30.00	48.59	5.40	3.06	93.96	22.82
NR-CdS	0.30	25.21	31.07	2.35	9.26	29.29	24.33
NR-CdS/NP-CdS	0.403	31.16	57.00	7.16	2.59	185.13	20.83
NP-CdS/NR-CDS	0.396	29.61	48.16	5.59	4.73	137.19	22.51

The external quantum efficiency (EQE) and integrated J_{SC} have been shown in Figure 5b. Although the NR-CdS device show improved blue response at a shorter wavelength (<500 nm), the NR-CdS/NP-CdS device provides the best spectral response at a wavelength range of 500-1100 nm among all the devices, indicating reduced recombination at the rear surface and enhanced carrier collection. The integrated J_{SC} from EQE measurement shows good agreement with the current density obtained by *J-V* measurement. The highest integrated J_{SC} of ~27.50

mA/cm^2 was obtained from NR-CdS/NP-CdS solar cell, whereas the lowest integrated J_{SC} of ~21.50 mA/cm^2 was acquired from NR-CdS solar cell. This enhanced integrated J_{SC} suggests improved carrier collection for the heterostructured NR-CdS/NP-CdS buffered Sb_2Se_3 device due to low carrier recombination because of the improved front (buffer/absorber) and rear (absorber/HTL) interface. Herein, the relative difference between J-V measured and EQE measured current density could be due to the use of low-intensity monochromatic light in EQE measurement. The deep level defect within the junction region was activated, and those deep levels work as a generation-recombination center, resulting in lower J_{SC} in EQE than J-V measured J_{SC}.[26, 27] To further examine the carrier collection improvement in NR-CdS/NP-CdS buffered devices compared to other buffer layer-based devices, we measured the EQE of all devices with an applied bias voltage of -0.5 V. Figure 5c shows the ratio of EQE measured at -0.5 V and 0 V. The EQE (-0.5 V) / EQE (0 V) ratio in NR-CdS and NP-CdS devices is greater than 1, indicating that both devices require externally applied voltage to segregate excitons, i.e., poor carrier collection. Promisingly, heterostructured NR-CdS/NP-CdS and NP-CdS/NR-CdS buffer layer-based Sb_2Se_3 devices show EQE (-0.5 V) / EQE (0 V) ratio close to 1, suggesting improved carrier collection at the back surface due to more Sb_2Se_3 nanoribbons normal to the substrate. [28] The deep defects at the CdS/Sb_2Se_3 heterojunction interface and within the space charge region (SCR) are the main culprit for device performance deterioration, which arises due to the band tailing effects.[29, 30, 31] To measure the extent of this band tailing in all devices, we extracted the Urbach energy (E_U) by plotting the ln(-ln(1-EQE)) *versus* the energy curve, shown in Figure 5d. The value of E_U decreases from 24.33 meV to 20.83 meV after adding a layer of nanoparticles CdS on nanorods CdS, suggesting that the non-radiative recombination reduces in the heterostructured NR-CdS/NP-CdS device through possibly deep defects passivation.[32]

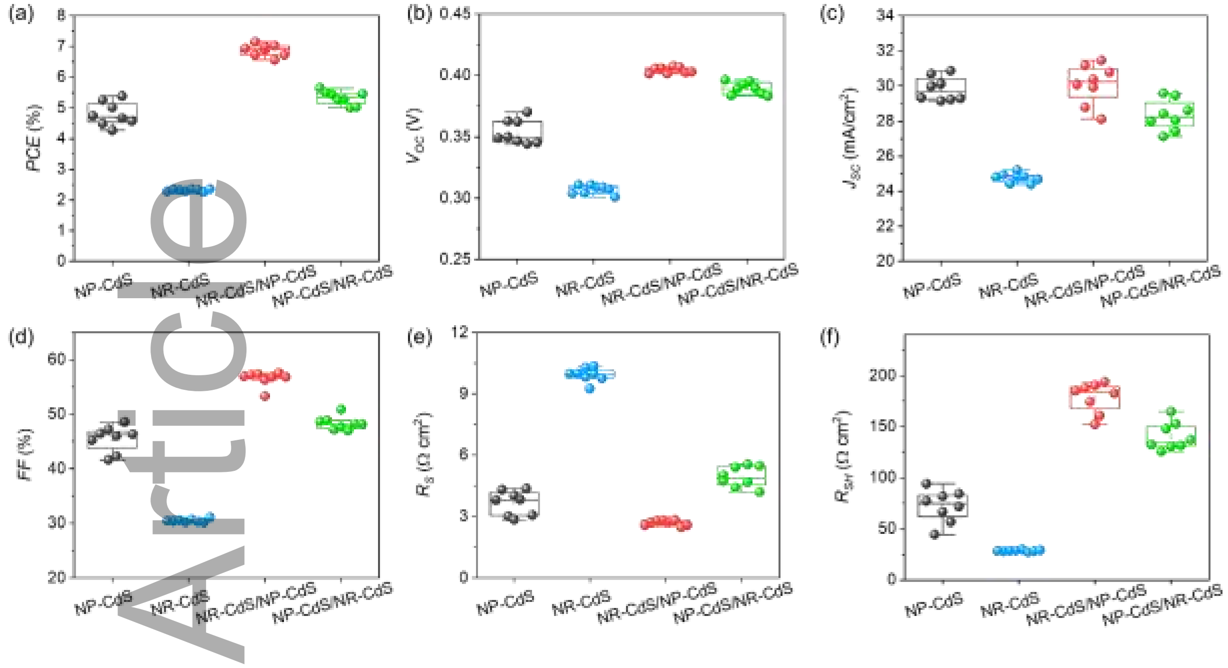

Figure 6. Statistical distributions of Sb_2Se_3 solar cell performance parameters with various CdS buffers: (a) power conversion efficiency (PCE), (b) open-circuit voltage (V_{OC}), (c) short-circuit current density (J_{SC}), (d) fill factor (FF), (e) series resistance (R_S), and (f) shunt resistance (R_{SH}).

The statistical distribution of the Sb_2Se_3 solar cell's performance parameters has been presented in Figure 6a-f. The efficiency enhancement in the heterostructured NR-CdS/NP-CdS buffer layer-based Sb_2Se_3 devices can be related to the significant improvement for all the device parameters in V_{OC}, J_{SC}, and FF. Moreover, the improvement in J_{SC} and FF can be related to the reduced series resistance, suggesting lower barrier potential in agreement with the XRD data that proves the [211] and [221] directional growth of Sb_2Se_3 nanoribbons on the NR-CdS/NP-CdS buffer.[12]

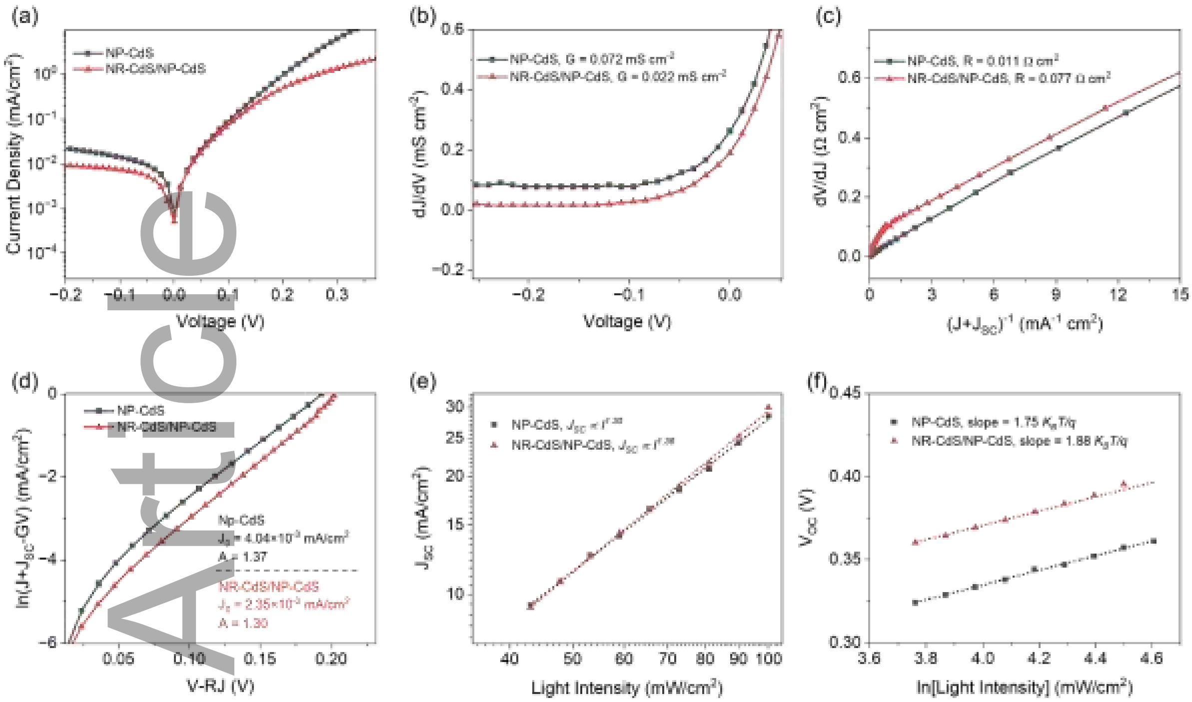

Figure 7. Electrical transport behavior of NP-CdS and heterostructured NR-CdS/NP-CdS based Sb_2Se_3 devices: (a) dark *J-V* curve, (b) shunt conductance *G* characterization, (c) series resistance *R* characterization, (d) diode ideality factor *A* and diode saturation current calculation from the $ln(J+J_{SC}-GV)$ vs. *(V-RJ)* plot, (e) J_{SC} versus light intensity, and (f) V_{OC} versus light intensity.

Figure 7a displays the dark *J-V* of the Sb_2Se_3 solar cell with NP-CdS and NR-CdS/NP-CdS buffer separately. The heterostructured NR-CdS/NP-CdS buffered device shows lower leakage current than the traditional NP-CdS buffered device, which originates from the lower Urbach energy calculated from EQE in NR-CdS/NP-CdS buffered device leading to less recombination loss (Figure 5d). To further confirm the lower leakage current and recombination loss in NR-CdS/NP-CdS device, we calculated the diode ideality factor and diode current from the dark *J-V* data by using the following diode equation of thin film solar cell. [33]

$$J = J_0 exp\left[\frac{q}{AKT}(V - RJ)\right] + GV - J_L \qquad (2)$$

Where J is the current density under V applied bias voltage, J_L=J_{SC}=0 (at dark), J_0 is the diode current, q is the electron charge, A is the diode ideality factor, K is the Boltzmann constant, T is the absolute value of room temperature (25 °C), R and G are the resistance and conductance extracted from the linear fitted curve. The extracted R and G have been shown in Figures 7b and c, where the heterostructured NR-CdS/NP-CdS buffered device shows a lower G of 0.022 mS cm^{-2} and higher R of 0.077 Ω cm^2 compared to the NP-CdS device G~0.072 mS cm^{-2} and R~0.011 Ω cm^2, indicating reduced leakage current due to higher barrier resistance in NR-CdS/NP-CdS buffered device. As shown in Figure 7d, the diode ideality factor and current have been calculated by using the G and R values in Equation 2 and plotting ln(J+J_{SC}-GV) versus (V-RJ) fitting curve. The value of A in the NP-CdS buffered device decreases from 1.37 to 1.30 after combing with the NR-CdS, suggesting improved diode behavior in NR-CdS/NP-CdS buffered device. Diode current J_0 reflects the recombination loss of a solar cell. Herein, the J_0 value of the NP-CdS buffered device reduces from 4.04×10^{-3} mA/cm^2 to 2.35×10^{-3} mA/cm^2 in NR-CdS/NP-CdS buffered device, justifying the reduced recombination loss in NR-CdS/NP-CdS buffered device. Furthermore, the lower A and J_0 of NR-CdS/NP-CdS buffered Sb_2Se_3 solar cell indicate that trap recombination in the space-charge region of the Sb_2Se_3 film controls the current, while trap recombination and tunneling-enhanced recombination both control the traditional NP-CdS/Sb_2Se_3 interface.[34, 35, 36] In addition to the diode properties analysis of the Sb_2Se_3 solar cell, we also measured J-V curves under various light intensities and plotted the J_{SC} and V_{OC} versus light intensity to get better insights into the recombination mechanism. Figure 7e represents the double logarithmic plot of J_{SC} versus light Intensity (I), which has been drawn according to the

$J_{SC} \propto I^{\alpha}$ power law dependence. When the device is free of space-charge limited photocurrent, the α value should be ~1. Since both NP-CdS and NR-CdS/NP-CdS buffered devices show α value greater than 1, indicating that both devices suffer from the space-charge limited photocurrent, and trap-assisted recombination. [34, 37] The V_{OC} has been plotted as a function of the natural log of light intensity, as shown in Figure 7f, according to the $V_{OC}(I) = \frac{nKT}{q}\ln(I) + Constant$ relationships. The slope *n* indicates loss mechanism due to recombination. If the *n* value is close to 2, the monomolecular (first-order) recombination is dominating, whereas if the *n* value approaches 1, the bimolecular (second-order) recombination is dominant. Therefore, both devices have monomolecular and bimolecular recombination, however, the bimolecular recombination was reduced in the case of the heterostructured NR-CdS/NP-CdS buffered device.[38]

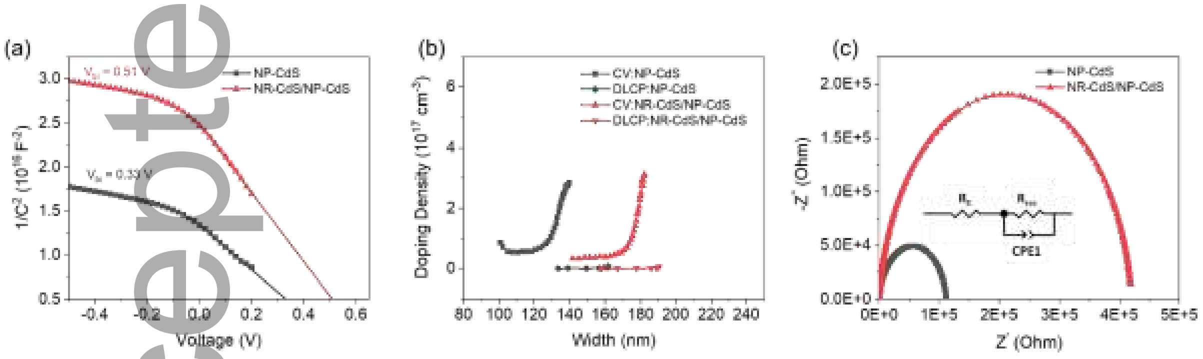

Figure 8. (a) Mott-Schottky plots, (b) C-V and DLCP profiling, and (c) EIS-derived Nyquist plot.

To better understand the interface electronic behavior in the heterostructured NR-CdS/NP-CdS buffered device, we performed the *C-V* and DLCP measurements to find the built-in potential (V_{bi}), defects, and depletion width. Figure 8a shows the Mott-Schottky plots (1/C^2 versus Voltage). The V_{bi} of the Sb_2Se_3 solar cell can be extracted from the X-intercept of the 1/C^2 versus Voltage curve. The V_{bi} of the NP-CdS device increases from 0.33 V to 0.51 V, which can be related to the improvement in V_{OC} in the NR-CdS/NP-CdS buffered device. In general, the doping density (Figure 8b) calculated from the C-V ($N_{C\text{-}V}$) data is the response from free carriers, bulk defects, and interface defects, whereas the doping density calculated from the DLCP (N_{DLCP}) data is only the response from free carriers and bulk defects. [28, 39] Therefore, the interface defects density of the Sb_2Se_3 solar cell can be determined from the difference between $N_{C\text{-}V}$ and N_{DLCP}. Figure 8b shows that the difference between $N_{C\text{-}V}$ and N_{DLCP} in NR-CdS/NP-CdS buffered device is lower than NP-CdS buffered device, demonstrating improved buffer/absorber interface through reduced defect density in the NR-CdS/NP-CdS buffered device. Moreover, the depletion width at zero bias voltage increases from 122.98 nm in NP-CdS buffered device to 167.03 nm in NR-CdS/NP-CdS buffered device, which can be attributed to the increased V_{bi} and reduced doping density. These enhanced V_{bi} and wider depletion region in NR-CdS/NP-CdS heterostructured buffered device benefits the carrier generation, and extraction, and thus enhances the overall device performance. [40]

In addition, the electrochemical impedance spectroscopy (EIS) measurement was carried out to analyze the interface charge transport properties in NR-CdS/NP-CdS buffered devices. Figure 8c presents the Nyquist plots of the impedance spectra for both Sb_2Se_3 solar cells with NP-CdS and NR-CdS/NP-CdS buffers, and the inset of Figure 8c shows the equivalent circuit used in the fitting of impedance data. Here, the R_s and R_{rec} represent series and charge recombination resistance respectively, and the CPE denotes a constant phase element. The R_{rec} of Sb_2Se_3 solar cell significantly increases from 1.12×10^5 Ω to 4.20×10^5 Ω when Sb_2Se_3 was deposited on NR-CdS/NP-CdS heterostructured buffer, indicating the charge recombination is greatly suppressed that eventually resulting in higher V_{OC} and J_{SC} in NR-CdS/NP-CdS solar cell.[39, 40] Conversely, the R_s decreases in NR-CdS/NP-CdS solar cells from 16.64 Ω to 12.11 Ω, suggesting easy carrier transportation due to the compact and vertical growth of Sb_2Se_3 ribbons on NR-CdS/NP-CdS buffer confirmed by XRD and SEM data.

3. Conclusion

In summary, we demonstrated that the heterostructured NR-CdS/NP-CdS buffer layer for the Sb_2Se_3 solar cell can significantly improve the device performance by tailoring the Sb_2Se_3 nanoribbon orientation normal to the substrate and optimizing the interface quality and carrier transport between buffer and absorber. The heterostructured NR-CdS/NP-CdS buffer can efficiently enhance the charge transport through CdS nanorods and Sb_2Se_3 nanoribbons and strongly diminish charge recombination by reducing the series resistance and increasing charge recombination resistance. A champion device performance of heterostructured NR-CdS/NP-CdS buffered Sb_2Se_3 solar cell with a power conversion efficiency of 7.16% has been achieved. This newly developed heterostructured CdS buffer layer provides an effective way to tailor the light absorber growth orientation while optimizing the interface to assist the photoexcited carrier collection in low-dimensional light absorber photovoltaic devices.

4. Experimental Section

Synthesis of the heterostructured CdS buffer layer: Cadmium sulfide nanoparticles (NP-CdS) buffer layers were deposited on the fluorine-doped tin oxide (FTO) coated soda-lime glass (TEC 10, NSG, US). Before the CdS deposition, the FTO substrate was cleaned with detergent, deionized water, acetone, and isopropanol in sequence in the ultrasonic bath for 30 minutes for each step. In addition, the FTO films were cleaned with UV ozone treatment for 30 minutes. The NP-CdS films were prepared by the traditional chemical bath deposition (CBD) method, where 0.015 M, 20 ml of cadmium sulfate $CdSO_4$ (Alfa Aesar, Anhydrous, ACS 99+%), 26 ml of 28-

30% NH_4OH (J. T. Baker), and 0.75 M, 10 ml of thiourea CH_4N_2S (Alfa Aesar, 99%) were subsequently added in a beaker with 146 ml of deionized water at ~70 °C under continuous stirring. Then FTO substrates were vertically placed in the chemical bath and continued deposition for around 15 minutes. After deposition, the FTO/NP-CdS films were washed with deionized water in ultrasonication for 10 minutes and dried by blowing dry air.

Nanorod CdS (NR-CdS) buffer layer was synthesized by a hydrothermal method on the FTO substrate. The precursor solution for NR-CdS synthesis was composed of 14.41 mM of cadmium nitrate tetrahydrate $Cd(NO_3)_2.4H_2O$ (Alfa Aesar, 99.999%), 57.64 mM of thiourea, and 8.65 mM of L-Glutathione (Alfa Aesar) in a Teflon container with 30 ml of deionized water. The solution was vigorously stirred until all chemicals were mixed properly and formed a transparent solution. After that, the cleaned FTO substrate was immersed in the prepared solution and tilted at an angle of 75°. Then the autoclave was sealed with a connected thermocouple to monitor the real temperature and placed inside a gravity box oven at 250 °C. Almost 40 minutes were needed to reach the autoclave temperature at 200 °C, then the hydrothermal reaction was further continued for 5 minutes. After the reaction was done, the autoclave was taken outside of the oven and naturally cooled down to room temperature. Finally, the FTO/NR-CdS film was cleaned in an ultrasonic bath for 5 minutes and dried with dry air.

Two more heterostructured buffers were synthesized with the combination of NP-CdS and NR-CdS. For the heterostructured NR-CdS/NP-CdS buffer layers, the NR-CdS layer was firstly deposited on the FTO substrate, following the NP-CdS layer was coated on the NR-CdS by CBD method at 70 °C for 5 minutes. For the heterostructured NP-CdS/NR-CdS buffer layer, CBD-grown NP-CdS layer was deposited on the FTO substrate, and then NR-CdS was grown on NP-CdS using the hydrothermal approach. The thickness of all buffers was kept around 80 nm. In this experiment, all chemicals were in analytical grade and used as received without further purification.

Deposition of Sb_2Se_3 and solar cell fabrication: The Sb_2Se_3 absorber layer with ~600 nm thickness was deposited on the NP-CdS, NR-CdS, NR-CdS/NP-CdS, and NP-CdS/NR-CdS buffer layers separately by using the close-spaced sublimation (CSS) method, as reported previously[40]. Briefly, during CSS deposition, the bottom heater's (source) and top heater's (substrate) temperatures were controlled at 550 °C and 300 °C respectively whereas the chamber pressure was maintained at ~10 mTorr. After the growth of Sb_2Se_3 nanoribbons on all the buffer layers, the spiro-OMeTAD hole-transport material (HTM) was spin-coated on the Sb_2Se_3 absorber to reduce the electron-hole recombination, and enhance carrier transport at the back interface according to the method reported elsewhere.[2] Finally, carbon paste was doctor bladed on the spiro-OMeTAD to form a complete solar cell device with an active cell area of 0.08 cm^2.

Materials characterization and solar cell measurement: The crystallinity and growth nature of CdS buffers and Sb_2Se_3 absorber films were characterized by the X-ray diffraction (XRD) system (Philips X'Pert MRP) with Cu Kα radiation (λ = 1.5416 Å). The surface morphology and cross-section were characterized by the Apreo field emission scanning electron microscope (FE-SEM). The thickness of the film was measured from the cross-section SEM images. For optical bandgap calculation, the transmittance and absorbance spectra were measured by UV-vis spectroscopy (Shimadzu UV1800).

The solar cell performance parameters (current density, voltage, series, and shunt resistance) were measured by using a solar simulator (Newport, Oriel Class AAA 94063A, 1000 Watt Xenon light source) equipped with a source meter (Keithley 2420) at AM 1.5 G irradiation (100 mW/cm^2). A calibrated Si-reference cell and meter (Newport, 91150 V, certified by NREL) were used to calibrate the solar simulator before the measurement. The QE-T, Enli Technology solar cell spectra response measurement system was used to measure the external quantum efficiency (EQE). The capacitance-voltage (*C-V*) and drive level capacitance profiling (DLCP) measurement was performed in the dark at room temperature using a Keithley 4200 semiconductor parameter analyzer (Tektronix 4200A-SCS, USA). The Electrochemical impedance spectroscopy (EIS) measurement was conducted by Solartron Analytical 1260 impedance analyzer at a bias potential of 0.5 V in the dark with the frequency ranging from 1 Hz to 1 MHz.

Acknowledgments

This work is supported by National Science Foundation under contract No. ECCS- 1944374, CMMI-2226918, DMR 2127640, CMMI-2019473, and OISE-2153439, and USDA National Institute of Food and Agriculture, AFRI project award (contract# 2020-67022-31376).

Conflict of Interest

The authors declare no conflict of interest.

Data Availability Statement

The data that support the findings of this study are available from the corresponding author upon reasonable request.

References

[1] C. Breyer, D. Bogdanov, S. Khalili, D. Keiner, Springer New York, 2021.

[2] A. Amin, D. Li, X. Duan, S. N. Vijayaraghavan, H. G. Menon, J. Wall, M. Weaver, M. M. C. Cheng, Y. Zheng, L. Li, F. Yan, *Advanced Materials Interfaces* **2022**,

[3] S. Barthwal, R. Kumar, S. Pathak, *ACS Appl. Energy Mater.* **2022**, 5, 6545
[4] S. Rijal, D.-B. Li, R. A. Awni, C. Xiao, S. S. Bista, M. K. Jamarkattel, M. J. Heben, C.-S. Jiang, M. Al-Jassim, Z. Song, Y. Yan, *Adv. Funct. Mater.* **2022**, 32, 2110032
[5] C. Liu, S. Wu, Y. Gao, Y. Feng, X. Wang, Y. Xie, J. Zheng, H. Zhu, Z. Li, R. E. I. Schropp, K. Shen, Y. Mai, *Adv. Funct. Mater.* **2022**, 32, 2209601
[6] A. Mavlonov, T. Razykov, F. Raziq, J. Gan, J. Chantana, Y. Kawano, T. Nishimura, H. Wei, A. Zakutayev, T. Minemoto, X. Zu, S. Li, L. Qiao, *Solar Energy* **2020**, 201, 227
[7] Y. Zhou, L. Wang, S. Chen, S. Qin, X. Liu, J. Chen, D.-J. Xue, M. Luo, Y. Cao, Y. Cheng, E. H. Sargent, J. Tang, *Nature Photonics* **2015**, 9, 409
[8] C. Chen, D. C. Bobela, Y. Yang, S. Lu, K. Zeng, C. Ge, B. Yang, L. Gao, Y. Zhao, M. C. Beard, J. Tang, *Front. Optoelectron.* **2017**, 10, 18
[9] C. Chen, K. Li, J. Tang, *Solar RRL* **2022**, 6, 2200094
[10] Z. Duan, X. Liang, Y. Feng, H. Ma, B. Liang, Y. Wang, S. Luo, S. Wang, R. E. I. Schropp, Y. Mai, Z. Li, *Advanced Materials*, 34, 2202969
[11] H. Lei, J. Chen, Z. Tan, G. Fang, *Solar RRL* **2019**, 3, 1900026
[12] H. Cai, R. Cao, J. Gao, C. Qian, B. Che, R. Tang, C. Zhu, T. Chen, *Adv. Funct. Mater.* **2022**, 32, 2208243
[13] K. Shen, Y. Zhang, X. Wang, C. Ou, F. Guo, H. Zhu, C. Liu, Y. Gao, R. E. I. Schropp, Z. Li, X. Liu, Y. Mai, *Adv. Sci.* **2020**, 7, 2001013
[14] A. Amin, D. Li, X. Duan, S. N. Vijayaraghavan, H. G. Menon, J. Wall, M. Weaver, M. M.-C. Cheng, Y. Zheng, L. Li, F. Yan, *Adv. Mater. Interfaces* **2022**, 9, 2200547
[15] W. Wang, L. Yao, J. Dong, L. Wu, Z. Cao, L. Hui, G. Chen, J. Luo, Y. Zhang, *Adv. Mater. Interfaces* **2022**, 9, 2102464
[16] G. Li, Z. Li, X. Liang, C. Guo, K. Shen, Y. Mai, *ACS Applied Materials & Interfaces* **2019**, 11, 828
[17] R. Krautmann, N. Spalatu, R. Gunder, D. Abou-Ras, T. Unold, S. Schorr, M. Krunks, I. Oja Acik, *Solar Energy* **2021**, 225, 494
[18] S. Lu, Y. Zhao, C. Chen, Y. Zhou, D. Li, K. Li, W. Chen, X. Wen, C. Wang, R. Kondrotas, N. Lowe, J. Tang, *Adv. Electron. Mater.* **2018**, 4, 1700329
[19] L. Wang, D.-B. Li, K. Li, C. Chen, H.-X. Deng, L. Gao, Y. Zhao, F. Jiang, L. Li, F. Huang, Y. He, H. Song, G. Niu, J. Tang, *Nature Energy* **2017**, 2, 17046
[20] M. Sun, W. Fu, Q. Li, G. Yin, K. Chi, X. Zhou, J. Ma, L. Yang, Y. Mu, Y. Chen, H. Yang, *J. Cryst. Growth* **2013**, 377, 112
[21] M. A. Islam, M. S. Hossain, M. M. Aliyu, P. Chelvanathan, Q. Huda, M. R. Karim, K. Sopian, N. Amin, *Energy Procedia* **2013**, 33, 203
[22] A. S. Najm, H. S. Naeem, D. A. R. M. Alwarid, A. Aljuhani, S. A. Hasbullah, H. A. Hasan, K. Sopian, B. Bais, H. J. Al-Iessa, H. S. Majdi, A. J. Sultan, H. Moria, *Coatings* **2022**, 12, 1400
[23] C. Yang, S. Liu, M. Li, X. Wang, J. Zhu, R. Chong, D. Yang, W.-H. Zhang, C. Li, *Journal of Colloid and Interface Science* **2013**, 393, 58
[24] L. Guo, B. Zhang, Y. Qin, D. Li, L. Li, X. Qian, F. Yan, *Solar RRL* **2018**, 2
[25] L. Guo, B. Zhang, S. Ranjit, J. Wall, S. Saurav, A. J. Hauser, G. Xing, L. Li, X. Qian, F. Yan, *Solar RRL* **2019**, 3
[26] V. L. Dalal, A. R. Moore, *J. Appl. Phys.* **1977**, 48, 1244
[27] V. L. Dalal, A. Rothwarf, *J. Appl. Phys.* **1979**, 50, 2980

[28] Z. Li, X. Liang, G. Li, H. Liu, H. Zhang, J. Guo, J. Chen, K. Shen, X. San, W. Yu, R. E. I. Schropp, Y. Mai, *Nat Commun* **2019**, 10, 125

[29] Y. Gong, R. Qiu, C. Niu, J. Fu, E. Jedlicka, R. Giridharagopal, Q. Zhu, Y. Zhou, W. Yan, S. Yu, J. Jiang, S. Wu, D. S. Ginger, W. Huang, H. Xin, *Adv. Funct. Mater.* **2021**, 31, 2101927

[30] Z. Su, G. Liang, P. Fan, J. Luo, Z. Zheng, Z. Xie, W. Wang, S. Chen, J. Hu, Y. Wei, C. Yan, J. Huang, X. Hao, F. Liu, *Adv Mater* **2020**, 32, e2000121

[31] Y. Gong, Y. Zhang, Q. Zhu, Y. Zhou, R. Qiu, C. Niu, W. Yan, W. Huang, H. Xin, *Energy Environ. Sci* **2021**, 14, 2369

[32] R. Tang, S. Chen, Z.-H. Zheng, Z.-H. Su, J.-T. Luo, P. Fan, X.-H. Zhang, J. Tang, G.-X. Liang, *Adv. Mater.* **2022**, 34, 2109078

[33] S. S. Hegedus, W. N. Shafarman, *Prog Photovolt* **2004**, 12, 155

[34] K. Shen, Y. Zhang, X. Wang, C. Ou, F. Guo, H. Zhu, C. Liu, Y. Gao, R. E. I. Schropp, Z. Li, X. Liu, Y. Mai, *Adv Sci* **2020**, 7, 2001013

[35] H. Bayhan, A. S. Kavasoğlu, *Solid State Electron* **2005**, 49, 991

[36] U. Rau, *Appl. Phys. Lett.* **1999**, 74, 111

[37] X. Wen, C. Chen, S. Lu, K. Li, R. Kondrotas, Y. Zhao, W. Chen, L. Gao, C. Wang, J. Zhang, G. Niu, J. Tang, *Nat Commun* **2018**, 9

[38] F. Gao, Z. Li, J. Wang, A. Rao, I. A. Howard, A. Abrusci, S. Massip, C. R. McNeill, N. C. Greenham, *ACS Nano* **2014**, 8, 3213

[39] W. Wang, Z. Cao, L. Wu, F. Liu, J. Ao, Y. Zhang, *ACS Appl. Energy Mater.* **2021**, 4, 13335

[40] L. Guo, S. N. Vijayaraghavan, X. Duan, H. G. Menon, J. Wall, L. Kong, S. Gupta, L. Li, F. Yan, *Solar Energy* **2021**, 218, 525

Developing high-efficiency Sb2Se3 solar cells requires overcoming the challenge of controlling the orientation of nanoribbons. A heterostructured CdS buffer, comprising hexagonal nanorods and cubic nanoparticles, facilitates directional grain growth in CSS-grown Sb2Se3 film along the [211] and [221] directions. This reduces interface defects and recombination loss, resulting in an improved efficiency of 7.16%.